Evaluating Phase Histograms for Remote Sensing of Forested Areas Using L-Band SAR:Theoretical Modeling and Experimental Results

Chuanjun Wu, Stefano Tebaldini, *Senior Member, IEEE,* Marco Manzoni, *Member, IEEE,* Yanghai Yu, Mingsheng Liao

Abstract—This paper evaluates the recently introduced phase histogram (PH) technique for estimating forest height and vertical structure using theoretical modeling and synthetic aperture radar (SAR) data experiment, and makes comparison with the well-known SAR tomography (TomoSAR) technique. By jointly exploiting multiple SAR images, TomoSAR allows for direct imaging of the three-dimensional structure of the vegetation, from which biophysical parameters such as forest height and terrain topography can be extracted. The PH technique assigns each pixel in a SAR interferogram to a specific height bin based on the value of the corresponding interferometric phase, thus allowing for the estimation of the forest vertical structure by accumulating pixels magnitudes within a given spatial window. The two techniques are here compared on an experimental basis using monostatic L-Band tomographic data from the ESA campaign TomoSense, flown in 2020 at the Eifel Park in North West Germany, including 30 +30 monostatic overpasses acquired along two opposite flight headings. The analysis we present considers a characterization of forest scattering by 3D imaging and forest height retrieval. Experimental results indicate that the PH technique can only loosely approximate the vertical structure produced by SAR tomography. Still, it can produce a reasonably good estimate of forest height. In particular, TomoSAR and the PH technique are observed to have an average root mean square error (RMSE) with respect to Lidar estimate of 2.8 m and 4.45 m in North-West heading data, and 1.84 m and 5.46 m in South-East heading data, respectively. The observed results are interpreted in light of a simple physical model to characterize phase histograms depending on the number of scatterers within the SAR resolution cell, on which basis we derive analytical expressions to predict height dispersion in phase histograms. The conclusion from both experimental and theoretical results is that phase histograms cannot correctly reproduce forest structure, unless the distribution of scatterers within the SAR resolution cell is characterized by a single dominant scatterer. Consistently, we conclude that the PH technique is inherently best suited for the analysis of high- or very-high resolution data, which suggests its use in the context of higher frequency SAR Missions (e.g.: Tandem-X) and when there are few acquisitions available.

Index Terms—SAR, L-Band, SAR tomography, phase histogram, forest scattering, forestry

C. Wu and M. Liao are with the State Key Laboratory of Information Engineering in Surveying, Mapping and Remote Sensing, Wuhan University, Wuhan 430079, China(e-mail: wcj-sar@whu.edu.cn, liao@whu.edu.cn).

S. Tebaldini and M. Manzoni are with Politecnico di Milano, Milano 20133, Italy (e-mail: stefano.tebaldini@polimi.it, marco.manzoni@polimi.it).

Y. Yu is with National Space Science Center, Chinese Academy of Sciences, Beijing 100910, China(email:yuyanghai@nssc.ac.cn).

I. INTRODUCTION

FORESTS are crucial to understanding the terrestrial carbon cycle and its implications on climate change. For this reason, the scientific community has repeatedly stated the importance of the provision of accurate information about the world's forests [1]. In this context, the research carried out in the last years has demonstrated that observing the vertical structure of the vegetation plays a fundamental role in the retrieval of biophysical parameters such as forest height and Above Ground Biomass (AGB). This is largely witnessed by missions such as GEDI, which implements a Lidar sensor onboard the International Space Station, and BIOMASS, which will implement a P-Band spaceborne Synthetic Aperture Radar (SAR) and is tasked with measuring forest parameters globally and systematically [2]–[4].

Considering the specific case of SAR systems, different methods have been proposed to exploit the vertical structure of the vegetation for the retrieval of biophysical parameters. The well-known PolInSAR algorithm leverages polarization and baseline diversity to decompose the interferometric coherence into ground-only and volume-scattering contributions, after which forest height is retrieved based on suitable parametric model [5]–[8]. The recently proposed Ground Cancellation algorithm is based on a coherent cancellation of ground scattering by taking the difference between two phase-calibrated SAR images [9], [10]. SAR tomography (TomoSAR) synthesizes a two-dimensional aperture by collecting multiple flights over the same area, thus providing resolution also in the elevation direction. In this way, TomoSAR allows for direct imaging of the vertical structure of forest scattering, on which basis biophysical parameters are derived [11]–[25].

Quite interestingly, a different approach for retrieving information about the vertical structure of the vegetation is found in [26]–[28]. This approach, which we refer to as Phase Histogram (PH) technique, attempts to retrieve forest structure by analyzing the interferometric phase from a single interferometric pair within a given estimation window. Each pixel from a SAR interferogram is assigned to a specific height bin based on the value of the corresponding interferometric phase and the interferometric vertical wavenumber. In so-doing, a tomography-like representation of forest vertical structure is built by accumulating the intensity of all pixels that fall in the same height bin within a given spatial window [28].

The main goal of this paper is to understand the limits of

Fig. 1. Schematic diagram illustrating the TomoSAR acquisition geometry [29].

the PH technique and the main contributions of this paper are:

1) Using multi-polarized monostatic L-Band TomoSense data to analyze the performance of PH technique in reconstructing the vertical structure of the forest;

2) Introducing a new physical modeling of PH technique, and quantitatively characterizing the height dispersion of the phase histogram as a function of the number of scatterers within any SAR pixel.

To do that, we first compare the PH technique against TomoSAR on an experimental ground by analyzing L-Band tomographic data from the ESA airborne campaign TomoSense [17], flown in 2020 at the Kermeter area in the Eifel Park, North-West Germany. The data analyzed in this paper feature 30+30 mono-static overpasses acquired along two opposite flight headings, and provide a vertical resolution consistently better than 5 m on the whole area of interest. Moreover, the data are accurately calibrated and ground-steered, so that the phase reference for any interferogram is automatically set to 0 in correspondence of the terrain level [17]. The analysis we present considers the evaluation of the vertical profile of forest scattering and forest height retrieval. In the evaluation of the forest vertical profile, we take the result by TomoSAR as the auxiliary verification against which to evaluate the PH technique, by virtue of the fine vertical resolution ensured by TomoSense data. Certain areas of interest in leaf area density (LAD) products from terrestrial laser scanning (TLS) and airborne laser scanning (ALS) are taken as references. Concerning the estimation of forest height, both TomoSAR and the PH technique are evaluated against the canopy height model (CHM) generated by ALS. The observed results are interpreted in light of a simple physical model to characterize phase histograms depending on the number of scatterers within the SAR resolution cell, on which basis we derive analytical expressions to predict height dispersion in phase histograms.

The structure of this paper is as follows. In section II we recall signal processing models and methods for TomoSAR

and the PH technique. In section III we present the TomoSense data-set. Experimental results are shown in section III. Phase histogram modeling is presented in section V. Conclusions are drawn in section VI.

II. SIGNAL MODEL AND PROCESSING METHODS

This section is intended to present basic physical models underpinning the estimation of forest vertical structure from SAR data, and to recall the rationale of tomographic SAR imaging and the PH technique.

We consider the availability of a stack of N SAR images, correctly coregistered on a common grid and phase calibrated [29]. For sake of simplicity we consider here the case of approximately parallel trajectories[1], which allows to express the complex SAR pixel from the $n-th$ SAR image as [29]:

$$I_n\left(r,x\right) = \int_\Omega s(y,z)\exp\left(j\frac{4\pi}{\lambda}R_n(y,z)\right)dydz \quad (1)$$

where:

- the subscript Ω is used to remark that the integration is limited to the extent of the SAR resolution cell, defined by the range and azimuth resolution of the SAR system.
- $s(y,z)$ represents the complex reflectivity of the individual scattering elements in height/ground range plane.
- λ is the carrier wavelength.
- $R_n(y,z)$ denotes slant range, intended as the closest-approach distance between the ground objects at position (y,z) and the $n-th$ trajectory.

As commonly done in the literature, we define a reference topography and a reference (Master) flight, in such a way as to approximate the slant range distance for each image as:

$$R_n(y,z) = R_n(y_{ref},z_{ref}) + \frac{b_n}{R}v + r \quad (2)$$

where:

---

[1]We refer the reader to [16] for the case of non-parallel trajectories.

- (r, v) are the slant range and elevation coordinates w.r.t. the reference point (y_{ref}, z_{ref}). The reference point is assumed to lie on the terrain surface, which we assume to be known (e.g.: based on the availability of a Lidar DTM or tomographic processing [18], [30], [31]), see Fig. 1.
- b_n is the length of the normal interferometric baseline of the $n - th$ trajectory and R is the distance from the Master image and the reference point.

Plugging (2) into (1) and solving the integration with respect to r leads to:

$$I_n\left(r, x\right) = \exp\left(-j\frac{4\pi}{\lambda}R_n(y_{ref}, z_{ref})\right) \int p(v)\exp\left(jk_nv\right) dv \tag{3}$$

where $p(v)$ is the projection of the complex reflectivity $s(y, z)$ along elevation [29] and $k_n = \frac{4\pi b_n}{\lambda R}$ is the interferometric elevation wavenumber.

After terrain flattening, consisting in the removal of the phase terms outside the integral in equation (3), one finally gets that:

$$I_n^{TC}\left(r, x\right) = \int p(v)\exp\left(jk_nv\right) dv \tag{4}$$

where $I_n^{TC}\left(r, x\right) = I_n\left(r, x\right)\exp\left(j\frac{4\pi}{\lambda}R_n(y_{ref}, z_{ref})\right)$ denotes the stack of terrain compensated (TC) SAR pixels. We finally note that it is common practice to express equation (4) upon the change of variable $z = v \cdot sin\theta$, with θ the local incidence angle, so as to make direct reference to the vertical direction. In so-doing, we can finally state the fundamental model:

$$I_n^{TC}\left(r, x\right) = \int p(z)\exp\left(jk_z\left(n\right)z\right) dz \tag{5}$$

where the interferometric vertical wavenumber is:

$$k_z\left(n\right) = \frac{4\pi b_n}{\lambda R \sin\theta} \tag{6}$$

A. SAR tomography

SAR Tomography can be thought of as a straightforward extension of traditional SAR focusing from 2D to 3D. Conventional SAR systems transmit radar pulses and receive the echoes backscattered by the illuminated targets along the flight trajectory. In this way, the received signal can be focused to produce a 2D image of the illuminated area, where targets are resolved in the range/azimuth plane. TomoSAR imaging is based on the joint exploitation of multiple SAR images acquired along different tracks. This allows focusing the received signal not only in the range/azimuth plane, as in conventional 2D SAR imaging, but also in elevation [11], [12], [32]–[39]. A pictorial representation of how the TomoSAR technique works is provided in Fig. 1. On a mathematical ground, SAR Tomography is a sheer consequence of the model in equation (5). This model states that the stack of SAR pixels is obtained as the Fourier Transform of the vertical distribution of the projected reflectivity $p(z)$, which can therefore be reconstructed from the observed SAR data by Fourier analysis. This result has been exploited in number of

different contexts in the literature, leading to the development of various approaches depending on the particular case under investigation [16], [32], [39]–[42].

A most fundamental aspect that determines the quality of tomographic imaging is given by the distribution of the normal baselines, which determines the set of interferometric vertical wavenumbers k_z in equation (5). Following standard arguments from Fourier analysis, the achievable vertical resolution is given by the span of interferometric vertical wavenumbers that is:

$$dz = \frac{2\pi}{max\left(k_z\right) - min\left(k_z\right)} \tag{7}$$

This value is commonly referred to as Rayleigh resolution. Importantly, we recall here the existence of techniques that provide super-resolution capabilities, that is the capability to resolve targets at a finer resolution than the one expressed in (7). For forestry applications, super-resolution algorithms are typically needed whenever Rayleigh resolution is too coarse as compared to forest height, see for example [43]. Still, an aspect to be kept in mind is that super-resolution algorithms do not, in general, preserve radiometric accuracy, suggesting that the best option for tomographic imaging of forested areas is to design the acquisitions so as to guarantee a sufficiently fine Rayleigh resolution, as stated by equation (7). Since TomoSense L-Band data itself can provide a vertical resolution better than 5 m, the core of this paper is not to explore the application of super-resolution algorithms. Another fundamental parameter to the quality of tomographic imaging is represented by height of ambiguity (HoA), which represents the distance from a target along the vertical direction at which artifacts appear due to the finite sampling of the interferometric vertical wavenumbers. Assuming, for sake of simplicity, a uniform progression with spacing Δk_z the HoA is obtained as:

$$z_{amb} = \frac{2\pi}{\Delta k_z} \tag{8}$$

Common practice requires the HoA to be roughly twice forest height, see for example the case of the BIOMASS mission [4], implying that resolving n_l vertical layers within the vegetation requires no less than $2n_l$ acquisitions. The need for a large number of acquisitions is the real drawback of SAR Tomography. This is a possibility for airborne campaigns, where it is typically feasible to fly an aircraft many times in the same day. Still, it is indeed a most important hurdle towards spaceborne applications, where the number of available acquisitions corresponds to the number of orbits over a given area. As subsequent orbits are typically acquired at time lags of several days, the acquisitions are unavoidably degraded by temporal decorrelation, [44]–[47]. For this reason, the one mission currently appointed to gather tomographic acquisitions of forested areas is the forthcoming ESA Earth Explorer BIOMASS, for which temporal decorrelation is predicted to be successfully mitigated by the three-day revisit time and the long wavelength [48]. Besides addressing temporal decorrelation, most spaceborne SAR missions maintain a fixed orbit generating zero-baseline datasets, which are another problem for TomoSAR.
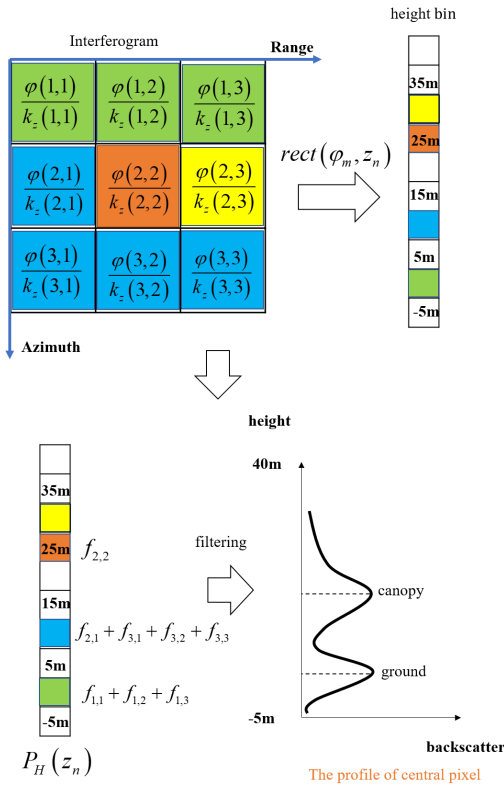
Fig. 2. Schematic diagram illustrating the implementation of PH technique.

B. Phase Histogram technique

Differently from SAR tomography, the Phase Histogram (PH) technique can - in principle - retrieve information about the forest structure by analyzing the interferometric phase from a single interferometric pair. This is obtained by assigning each pixel from a SAR interferogram within a given estimation window to a specific height bin based on the value of the corresponding interferometric phase and interferometric vertical wavenumber. In so-doing, a tomography-like representation of forest vertical structure is built by accumulating the intensity of all pixels that fall in the same height bin within a given spatial window [28].

Mathematically, the PH technique is described as follows. Let us consider a complex interferogram $\langle I_1^{TC}(m) \cdot conj\left(I_2^{TC}(m)\right)\rangle_L$, with the index m denoting the value of the $m-th$ pixel in the interferogram and the symbol $\langle\rangle_L$ denoting spatial averaging over L pixels (in case a multi-looked interferogram is used). Given an estimation window comprising $M > L$ pixels, the phase histogram is obtained as [28]:

$$P_H(z_n) = \sum_{m=1}^{M} f_m \cdot \text{rect}(\varphi_m, z_n) \qquad (9)$$

where:

- $P_H(z_n)$ is the value of the resulting phase histogram at height bin z_n.

- $\varphi_m = \angle\langle I_1^{TC}(m) \cdot conj\left(I_2^{TC}(m)\right)\rangle_L$ is the interferometric phase at the $m-th$ pixel.
- $\text{rect}(\varphi_m, z_n)$ represents a rectangle function of interferometric phase and height bin used to assign each pixel to a specific height bin. Formally:

$$\text{rect}(\varphi_m, z_n) = \begin{cases} 1, & \text{if } z_n - \frac{\Delta z}{2} < \frac{\varphi_m}{k_z} < z_n + \frac{\Delta z}{2} \\ 0, & \text{otherwise} \end{cases}$$
$$(10)$$

where Δz represents the height sampling interval and k_z is the interferometric wavenumber of the selected interferogram.

- f_m is a positive-valued term to be accumulated at each height bin. Different choices are reported in literature for this term. After the work in [28], we will here assume f_m to correspond to the magnitude of the (multi-looked) interferogram, i.e.: $f_m = \left|\langle I_1^{TC}(m) \cdot conj\left(I_2^{TC}(m)\right)\rangle_L\right|$.

A pictorial representation of how the PH technique works is provided in Fig. 2. In this paper, we employ single-look process to derive the interferometric phase. As the literature [27] indicates, the principle of "few look" plays a pivotal role in preserving the forest vertical structure and effectively discerning the ground. Consequently, we adopt the parameter $L = 1$ to extract the interferometric phase, facilitating a more precise representation of the forest's vertical composition. A comparison between single- and a multi-look processing will be discussed in later sections.

III. STUDY SITE AND DATASET

The TomoSense experiment was funded by ESA to support scientific research in the field of remote sensing of forested areas, with a particular emphasis on the application of To-moSAR methods in the context of future mono- and bi-static spaceborne missions operating at P-, L-and C-Band. The test site for the TomoSense experiment is the Kermeter area at the Eifel National Park in North Rhine-Westphalia, North-West Germany. SAR data include P-, L-, and C-Band surveys acquired by flying up to 30 trajectories in two headings to provide tomographic imaging capabilities. L- and C-Band data were acquired by simultaneously flying two aircraft to gather bistatic data along different trajectories. The SAR dataset is complemented by 3D structural canopy measurements made via terrestrial laser scanning, Unoccupied Aerial Vehicle Lidar (UAV-L), ALS, and in-situ forest census. All data are publicly available through ESA for the purpose of scientific research. The remainder of this section presents an overview of the test site and the collected SAR data. For a more detailed description of the TomoSense campaign and all acquired data we refer the reader to [17].

A. Test site

A photo of the Kermeter area is shown in Fig. 3, The location was chosen due to its abundant ecological diversity, characterized by forests that encompass a variety of species, diverse topography, and varying age classes. The Kermeter is an upland region, with an elevation range from 250 m to 530 m. The area is covered by one of the largest contiguous,

Fig. 3. The Kermeter area at the Eifel National Park, North-West Germany.

TABLE I: The parameters of mono-static L-Band dataset

Parameter	Value
Number of passes in NW	30
Number of passes in SE	30
Polarimetric channel	Full
Heading	NW and SE
Wavelength	21.8 cm
Bandwidth	50 MHz
Slant range resolution	3 m
Azimuth resolution	1 m
Vertical resolution	< 5 m

deciduous forests in that region. It covers an area of 3592 ha, of which about 3300 ha is a single forested area. Beech woods dominate the shaded, damp northern slopes (24%), in places with trees that are over 200 years old. Oak woods hold sway on the drier, southern slopes (26%), interrupted by rocky outcrops. About 550 ha consist of spruce trees, which are a consequence of reforestation measures after the Second World War. The main area of interest for SAR acquisitions is approximately 6.4 Km long and 800 m wide. Forest height ranges roughly from 10 to 30 m, with peaks up to over 40 m, whereas forest biomass ranges from 20 to 300 Mg/ha, with peaks up to over 400 Mg/ha. Topographic slopes at this area are typically on the order of $5°$, with few areas reaching $10°$ and beyond.

B. SAR data

SAR acquisitions were carried out by MetaSensing in 2020 (P- and L-Band) and 2021 (C-Band). The data were acquired by flying up to 30 times along two opposite headings (North-West and South-East), to provide vertical resolution capabilities from two opposite views. L- and C-Band data were acquired in bistatic mode by flying two identical SAR sensors onboard two aircraft. All data were collected in fully polarimetric mode, resulting in the collection of approximately one thousand SAR images. All data were focused in ground coordinates onto a Digital Terrain Model (DTM) available from aerial Lidar data by CzechGlobe. Data processing consisted in SAR focusing, phase calibration, terrain detection, and generation of tomographic products. Importantly, phase calibration of SAR data included accurate ground-steering, so that the phase of all interferograms is expected to be 0 in correspondence of the terrain level. We refer the reader to [17] for further details on signal processing of TomoSense data.

The data-set considered within this paper is the one acquired at L-Band in mono-static mode. This data-set includes 30 trajectories acquired along two opposite headings and guarantees a vertical resolution of 5 m or better across the whole area of interest. Specific SAR parameters for this data-set are reported in Table I.

C. Lidar data

The SAR data is complemented by small-footprint Lidar ALS data acquired by CzechGlobe in the summer 2018 and remeasured in the summer 2021. Lidar-derived products include terrain topography, forest height, and AGB estimates at 1 m posting. For the aim of providing a reference map to validate forest height retrieval, Lidar forest height map was further processed to make its spatial resolution comparable with that of SAR-derived products. This was done by taking the 75% percentile height within the estimation window used for SAR analysis (see next section). The derived forest height map was then resampled on the same spatial grid used for focusing SAR data. Importantly, we note that Lidar and SAR products were processed using the same terrain elevation as reference (i.e.: the one derived from Lidar), which reduced the conversion from one coordinate system to the other to a simple roto-translation.

IV. EXPERIMENTAL RESULTS

The analyses we present concern the evaluation of the vertical profile of forest scattering and the forest height retrieval. In the evaluation of the forest vertical profile, we take the result by TomoSAR as the reference against which to evaluate the PH technique by virtue of the fine vertical resolution ensured by TomoSense data. Concerning the estimation of forest height, both TomoSAR and the PH technique are evaluated against the canopy height model (CHM) generated by Airborne Laser Scanning.

A. 3D imaging of the vegetation

To ensure an objective and fair comparison between the two techniques, the LAD profiles acquired by TLS and ALS are adopted as references in this paper. We selected three plots with a 25 m radius (red circles in Fig. 9) and some specific areas of interest along the azimuth axis for comparative experiments. For data processing, we adopted the same window size for estimating the vertical distribution of the backscattered power by TomoSAR and for calculating the phase histograms. The window size is fixed to 35 m in ground range and 35 m in azimuth. The PH technique was implemented as described in section II-B using three levels of interferogram multilooking, namely $L = 1$ (i.e.: single look) and $L = 15$ (3 looks in ground range and 5 looks in azimuth), and $L = 119$ (7 looks in ground range and 17 looks in azimuth). For clarity, in the following, we will refer to phase histograms by the names *single-look PH* and *multi-looked PH*.

Phase histograms were built over an azimuth strip of approximately 3 Km by using 10 different interferometric pairs, which were selected so as to have a HoA between 60 m
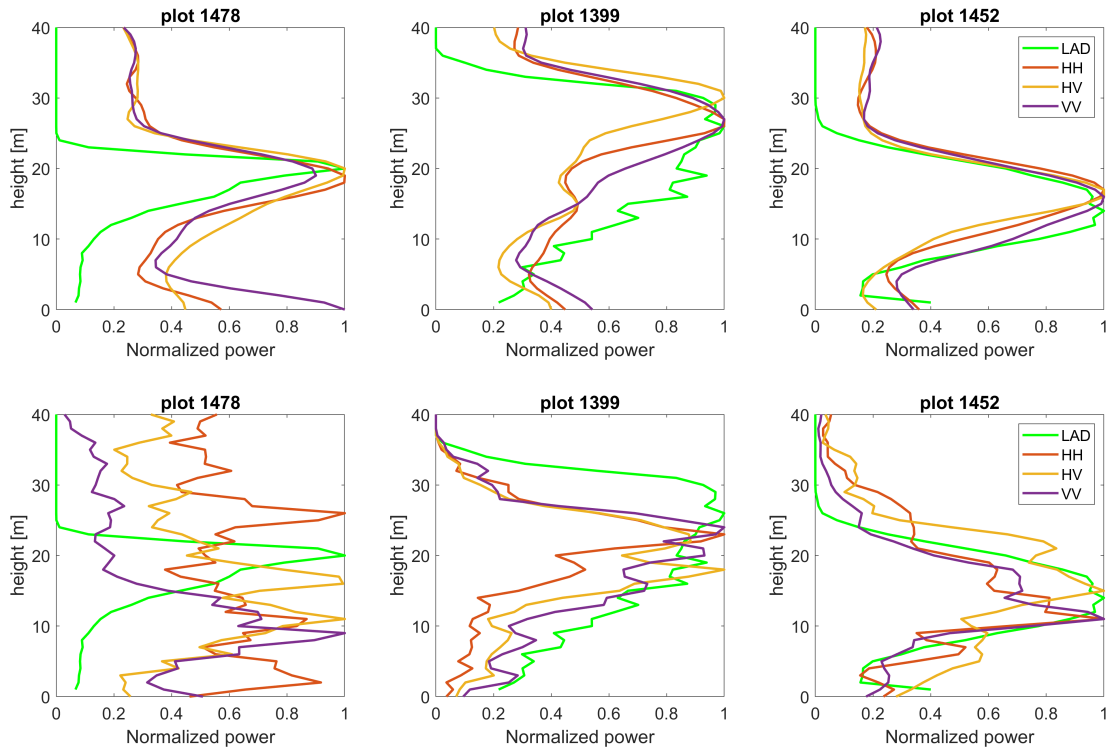
Fig. 4. Comparison between the backscattering profiles at all polarization and the LAD profiles of TLS data. Top panel: SAR Tomography. Second panel: the single-look PH technique. All panels are normalized from 0 to 1. These plots refer to the locations specified in NW Lidar CHM of Fig. 9.

and 100 m. This choice was necessary to counteract the large along-track baseline variations within the TomoSense dataset, which made it impractical to use a single interferogram to cover the whole analyzed area. The nominal incidence angle for the analyzed area is about 35°, which leads to a ground-range resolution of approximately 6 m.

SAR tomography was implemented on the same area by standard beamforming, namely:

$$T\left(z\right) = \left\langle \left| \sum_n I_n^{TC} exp\left(-jk_z\left(n\right)z\right) \right|^2 \right\rangle_W \qquad (11)$$

with $\langle\rangle_W$ denoting spatial averaging within the 35 × 35 m window. The choice of using beamforming is the consequence of the availability of a very large number of trajectories within the TomoSense dataset, which allows for fine vertical resolution (5 m or better) everywhere in the scene. For the same reason, within this section, we take the result from tomography as the auxiliary verification against which to evaluate results from the PH technique in this section. Certain areas of interest in LAD products from TLS and ALS are taken as references. Both techniques were used to generate 3D data over the selected area, which were afterwards resampled to move voxels above the ground to their correct ground-range position. This operation is essential to correctly compare 3D SAR data with the Lidar forest height map, especially in cases such as TomoSense characterized by a hilly topography.

Results comparing LAD profiles based on plot levels acquired by TLS with those obtained using both TomoSAR

and the single-look PH technique are illustrated in Fig. 4. These plots refer to the locations specified in NW Lidar forest height of Fig. 9. It can be clearly seen from the results that SAR tomography can match the LAD profiles very well, and can detect the accurate canopy phase center regardless of the polarization. Moreover, the energy attenuation and angular spread trends are also very similar. In contrast, with PH technique, the backscattering profile obtained is not always satisfactory. From the results of the three plots, the phase center peak positions obtained by different polarizations are not uniform, and there are obvious side lobes, especially in plot 1478. From the perspective of PH technique model (as shown in 9), the result is constrained by variations in both amplitudes and phase heights of adjacent pixels within the window. This limitation leads to the presence of more unwanted side lobes in the phase histograms along the vertical height axis when there are more than one dominant scatterers present in different horizontal height layers.

Results from multiple polarization relative to a single vertical section are shown in Fig. 5 and Fig. 6. The results from SAR tomography in Fig. 5 are quite clear and simple to interpret along the whole transect. Scattering from the terrain level is well detected, and the higher peak is observed to match Lidar canopy height in all the polarizations.

The multi-polarized results from the single-look PH in Fig. 6 are observed to produce a less clear result in any polarization. Some resemblance with the result from SAR tomography is observed, but overall the histogram appears to be dispersed along the height direction, providing no clear identification of
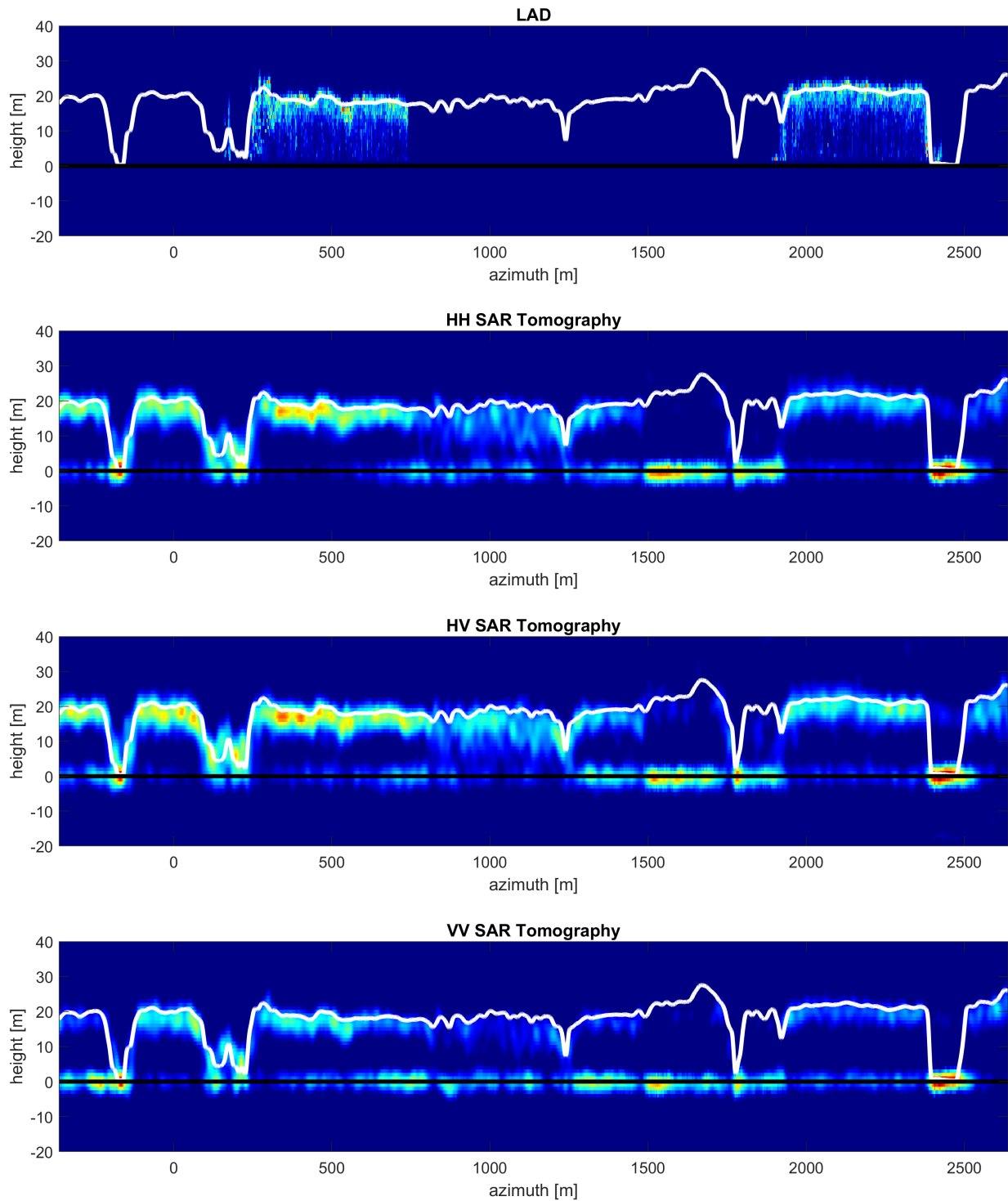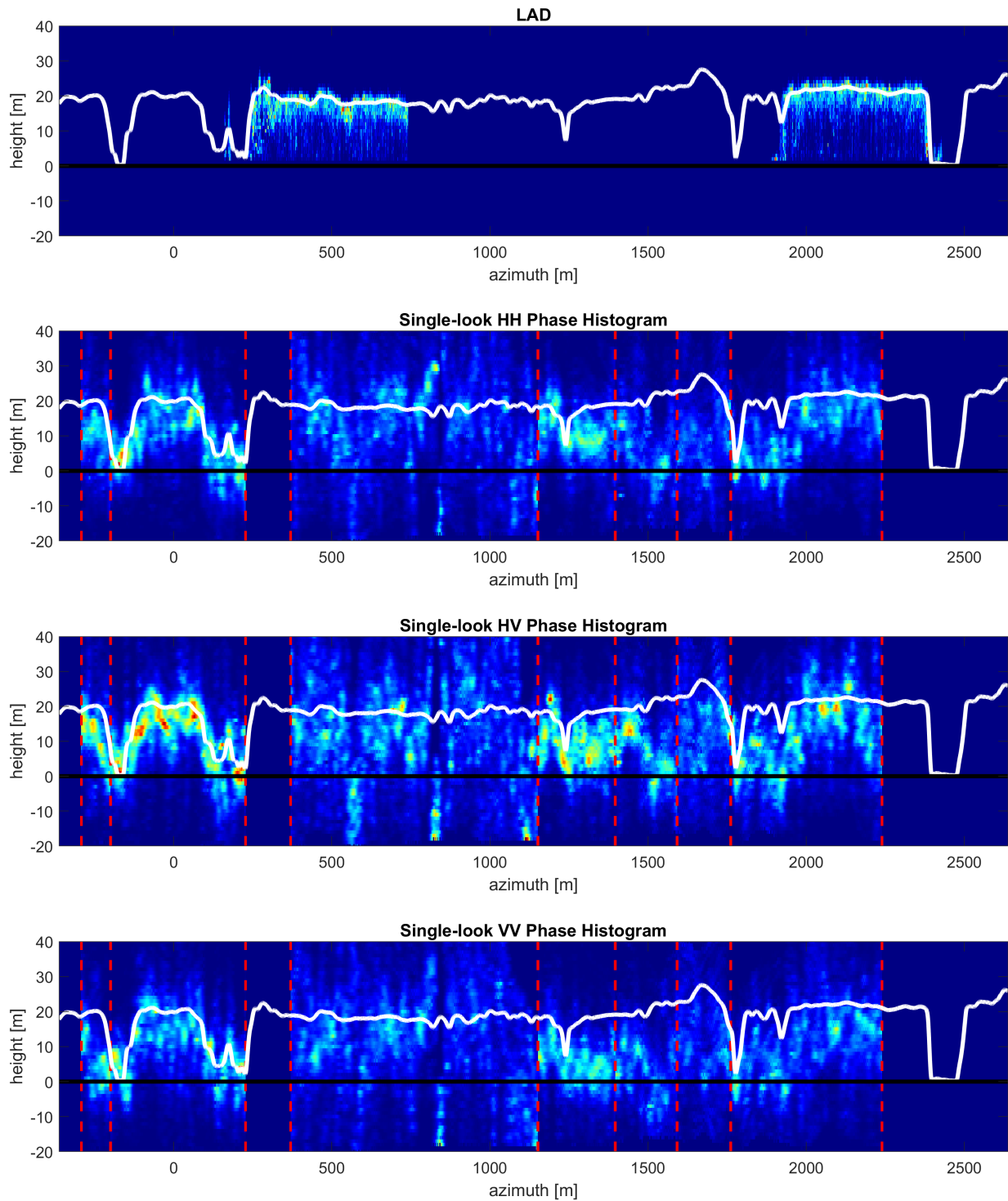
Fig. 5. Vertical section from TomoSAR technique. First panel from top: LAD profiles. Second panel from top to bottom: HH tomogram,HV tomogram and VV tomogram. All panels of tomograms are normalized such that the mean along each column is 1. In all panels, the white line denotes Lidar forest height and the black line denotes ground level.

scattering from the terrain and canopy layers. Moreover, the power peak along the vertical direction is generally observed to be at a lower location than the upper peak in the tomogram (hence below canopy height). Analyzing the outcomes, we observe that diverse polarizations yield similar results within either TomoSAR or the PH technique. This similarity could be

attributed to the penetrability of the L-Band and the scattering mechanisms within the forest. Nevertheless, our experimental findings demonstrate the superior capability of the TomoSAR technique over the PH technique in reconstructing the vertical structure of the forest.

Results relative to a single vertical section with multi-looked

Fig. 6. Vertical section from the PH technique. First panel from top: LAD profiles. The followed panels from top to bottom: HH phase histograms, HV phase histograms and VV phase histograms. All panels of phase histograms are normalized such that the mean along each column is 1. In all panels, the white line denotes Lidar forest height and the black line denotes ground level. The dashed red lines indicate the region covered by any single interferogram.

interferogram of the PH technique are shown in Fig. 7. The dispersion is reduced in the second panel from top, obtained by multilooking the interferogram with $L = 15$ looks. This is expected because the multi-looked interferogram will smooth the interferometric phase, leading to more concentrated phase histograms. This phenomenon becomes more apparent in the results when using a larger filter window, as shown in the bottom panel. This result is consistent with the recommendation in [27] to adopt a few-look approach when filtering interferograms, as it determines a balance between preserving
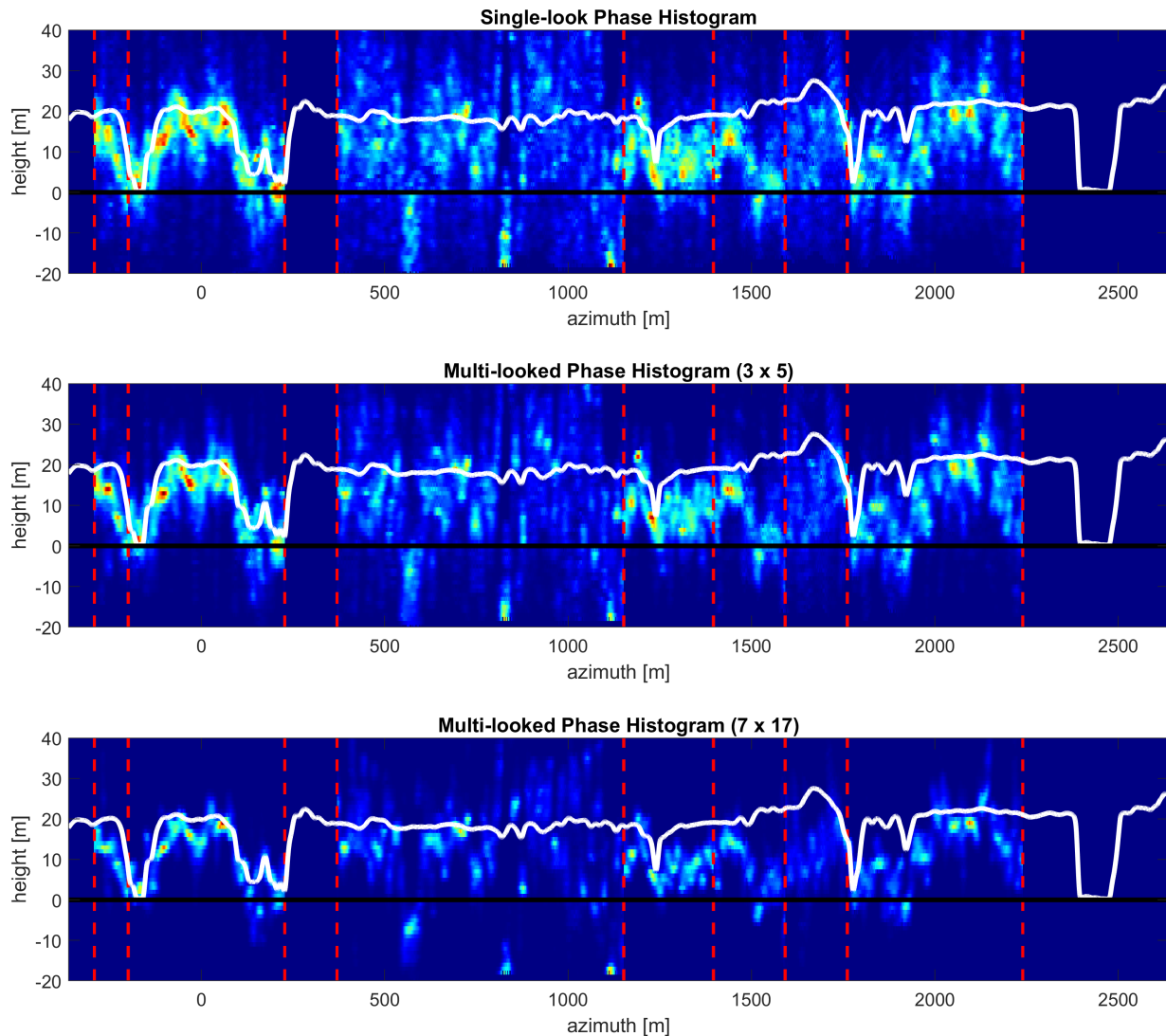
Fig. 7. Vertical section from the PH technique using multi-looked HV interferograms. First panel from top: single-look phase histogram. Second panel from top: multi-looked phase histograms (3×5 looks). Third panel from top: multi-looked phase histograms (7×17 looks). In all panels, the white line denotes Lidar forest height. All panels are normalized such that the mean along each column is 1. The dashed red lines indicate the region covered by any single interferogram.

relevant information and suppressing unwanted noise. As in the case of the single-look interferogram, the signal appears to peak at a lower height w.r.t. the tomogram, and scattering from the terrain level is undetected. Using a strong multilooking (bottom panel), the interferometric phase tends to default to the effective phase center within the estimation window. This is reflected in the phase histogram being concentrated at a single location in the vertical direction, often found in between terrain and canopy height.

To explore the role of spatial resolution on tomography and phase histograms, a further analysis is conducted after degrading the spatial resolution of complex SAR images to 12× 12 m (ground range× azimuth). Results are shown in Fig. 8. It is readily observed that the result from SAR tomography is essentially unchanged, as also in this case, it is possible to clearly detect scattering from the terrain and from the forest canopies. The result from the PH technique appears to show a

similar spatial characteristic as compared to the full-resolution case presented in Fig. 7, although showing a slightly higher dispersion along the vertical direction. Interestingly, the low-resolution PH presents few bright pixels within the forest layer, which are most likely associated with strong scatterers dominating the Radar returns at specific locations.

B. Forest height retrieval

Forest height retrieval was carried out over the entire area of interest by applying the power loss method in [13] to extract the upper envelope of the vertical structures produced by TomoSAR and the PH technique. The power loss method proceeds by selecting Lidar forest height as the ground truth, and then fit a proper power loss value for the forest height inversion of the entire scene. For the case of the PH technique, phase histograms at each location were built by processing the interferogram whose height of ambiguity was the closest to
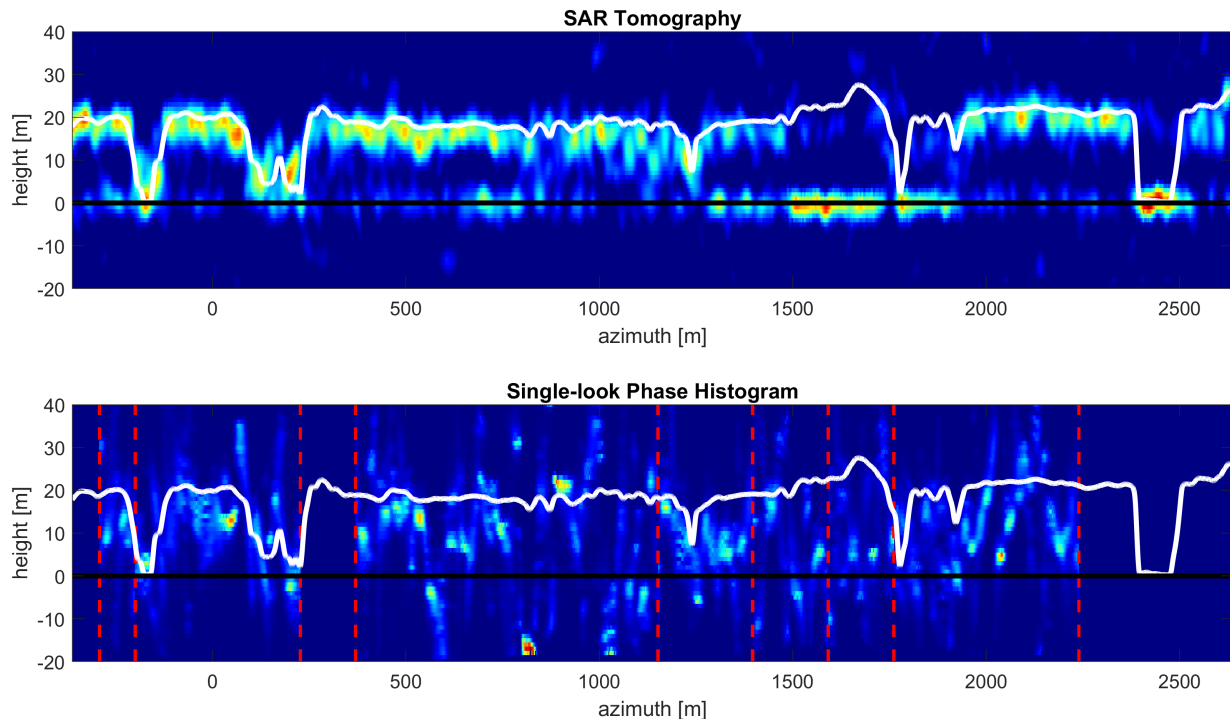
Fig. 8. Vertical section from TomoSAR and the PH technique as obtained from degraded resolution HV data. First panel from top: SAR Tomography. Second panel from top: single-look phase histogram. In all panels, the white line denotes Lidar forest height. All panels are normalized such that the mean along each column is 1. The dashed red lines indicate the region covered by any single interferogram.

the value of 60 m. The availability of $N = 30$ acquisitions allowed for the formation of $\frac{N(N-1)}{2} = 435$ interferograms at each image pixel, which made it possible to obtain the desired height of ambiguity everywhere in the scene with a deviation of few meters. The estimation window was set to 15×15 m for both TomoSAR and the PH technique.

Results are shown in Fig. 9 and Fig. 10 for the NW and SE data-sets, respectively. SAR tomography is observed to produce accurate results, achieving an overall RMS error of 2.8 m (NW dataset) and 1.84 m (SE dataset). The PH technique is not as accurate, attaining an overall RMS error of 4.45 m (NW dataset) and 5.46 m (SE dataset). Still, it succeeds in representing the variation of forest height over the whole scene. Completely wrong results are observed only in a few areas. Importantly, we remark that TomoSense data were already accurately ground-steered using tomographic methods, see [17]. For this reason, results relative to the PH technique are to be intended as lower bounds, terrain detection being already solved for this dataset.

V. MODELLING PHASE HISTOGRAMS

The observations from the previous paragraph indicate that the PH technique does provide an indication about forest structure, but it cannot be considered as effective as SAR tomography. This finding is to be compared to the the ones obtained at X-Band in [49] and [27] as well as from the ones in [28] at L-Band, where phase histograms could be effectively used for the detection of the terrain phase and the retrieval of forest height. Our interpretation of the observed results is

that the effectiveness of the PH technique is strictly related to the physics of forest scattering in SAR data, as determined by wavelength and spatial resolution. For an X-Band high-resolution system it is plausible to assume that the the Radar returns are dominated by single scatterers, either within the forest canopies or even at the ground level by penetration through forest gaps. In such a situation, the interferometric phase in each pixel is mostly associated with the height of the dominant scatterer, resulting in a clear phase signature. This interpretation is consistent with the one in [50], which suggests that high-resolution X-Band data are characterized by high extinction and large gaps that allow significant penetration. On the other hand, at lower frequencies the SAR pixel is more likely to be determined by a multitude of elementary scatterers, as a result of the penetration capabilities of longer wavelengths. In this situation the value of the interferometric phase at each SAR pixel is determined by the interference among all scatterers within the same resolution cell, triggering a random behavior. This phenomenon is clearly also related to spatial resolution, in that a coarser spatial resolution increases the possibility to have multiple scatterers within a single SAR pixel. Still, it is important to recall that scattering at longer wavelength is also determined by dominant scatterers. This is for example the case of ground-trunk double bounce scattering, especially at P-Band [51], but it might as well be associated with scattering from (well-oriented) large branches within forest canopies.

Based on this discussion, the comparison between SAR tomography and the PH technique presented in the previous
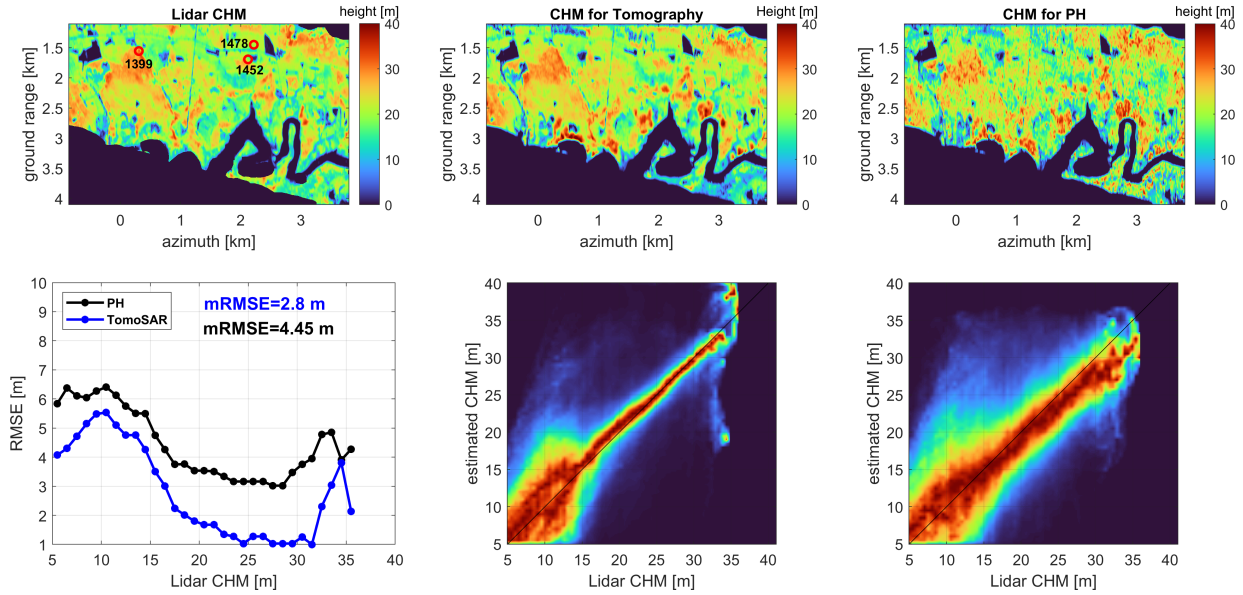
Fig. 9. Forest height retrieval for NW acquisitions. Top row: canopy height model (CHM) from Lidar, TomoSAR, and the PH technique. Bottom row: resulting RMS error (left panel) and 2D histograms of Lidar CHM and the retrieved height from TomoSAR (mid panel) and the PH technique (right panel).
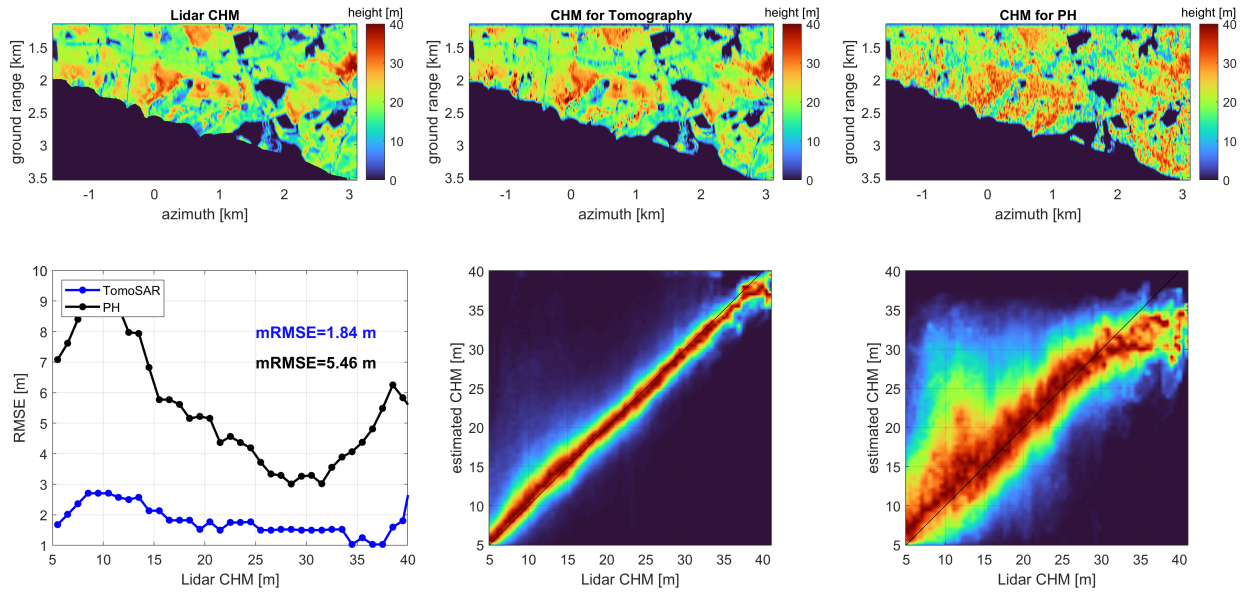

Fig. 10. Forest height retrieval for SE acquisitions. Top row: canopy height model (CHM) from Lidar, TomoSAR, and the PH technique. Bottom row: resulting RMS error (left panel) and 2D histograms of Lidar CHM and the retrieved height from TomoSAR (mid panel) and the PH technique (right panel).

section seems to indicate that L-Band TomoSense data respond better to the multiple scatterer model in (5), in particular: i) we ascribe the absence of a detectable signal from the terrain in PHs to the complex topography that characterizes TomoSense data, which inhibits strong reflection from the ground level; ii) the observation that PHs are dispersed along the vertical direction and peak at a lower height w.r.t. SAR tomography suggests that canopy scattering is not, in general, characterized by dominant scatterers.

To substantiate the discussion, we develop here a simple mathematical model derived by discretizing equation (5) to

express the SAR pixels in two images as a collection of elementary scatterers. We assume the scatterers to have unitary amplitude, so as to describe a situation where no dominant scatterer is present, whereas the phase of each scatterer is assumed to be uniformly distributed in the interval $(-\pi, +\pi)$ to account for the fact that the range to each scatterer may vary by several wavelengths within the resolution cell. With
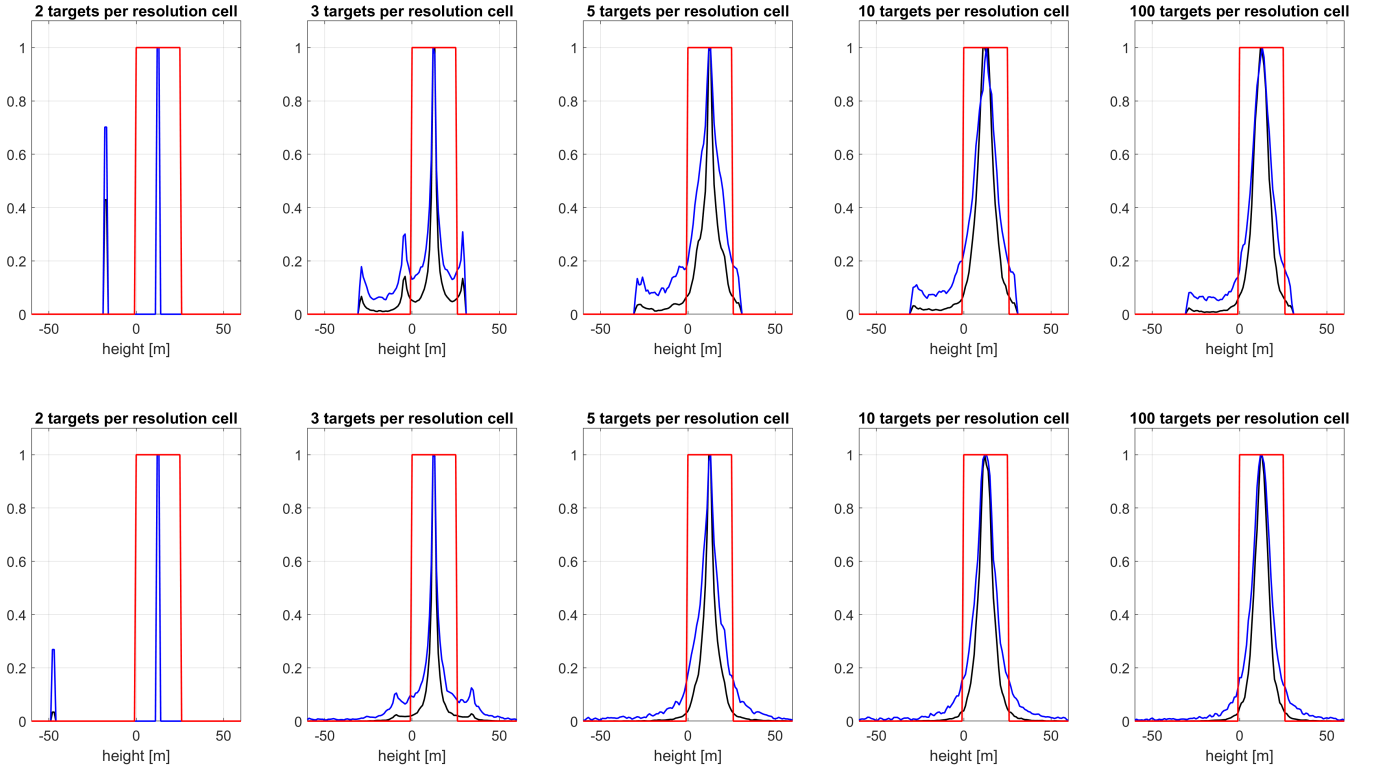
Fig. 11. Single-look phase histograms from numerical simulations assuming a number of point targets varying from 2 to 100. In all other experiments the targets are uniformly deployed in a region from 0 m to 25 m, indicated by the red rectangles. The height of ambiguity is fixed to 60 m in all experiments in the top row and 120 m in all experiments in the bottom row. Each histogram is obtained from 10^5 independent realizations. Blue curves were obtained by accumulating unitary values, that is by letting $f_m = 1$ in equation (9). Black curves were obtained by accumulating interferogram amplitudes.

those assumptions, the model is given as:

$$I_1^{TC} = \sum_{n=1} exp\left(j\psi_n\right) \tag{12}$$

$$I_2^{TC} = \sum_{n=1} exp\left(j\psi_n\right) \cdot exp\left(jk_z z_n\right)$$

with k_z is the interferometric wavenumber of the image pair. The interferogram is $X = I_2^{TC} \cdot conj\left(I_1^{TC}\right)$, which we rewrite as:

$$X = \sum_{n,m} exp\left(j\left(\psi_n - \psi_m\right)\right) \cdot exp\left(jk_z z_n\right) \tag{13}$$

$$= \sum_{n} exp\left(jk_z z_n\right) + \sum_{n \neq m} exp\left(j\left(\psi_n - \psi_m\right)\right) \cdot exp\left(jk_z z_n\right)$$

The second term in the second equation (the double sum for $n \neq m$) is a random number that describes the interference among all targets within the resolution cell, determining phase dispersion. Note that this term vanishes in expectation (hence it tends to vanish by multilooking), so that the expected value of the interferogram is:

$$E\left[X\right] = \sum_{n} exp\left(jk_z z_n\right) \tag{14}$$

This term is deterministic number, whose phase determines the interferometric phase center:

$$z_{pc} = \frac{\angle E\left[X\right]}{k_z} \tag{15}$$

Assuming a collection of 2 or more scatterers uniformly distributed in the height interval $(0, z_{max})$, the interferometric phase center is readily found to correspond to the center of the distribution, i.e.: $z_{pc} = \frac{z_{max}}{2}$.

To visualize the effect of phase dispersion, we report in Fig. 11 the phase histograms resulting from Monte Carlo experiments obtained by implementing the interferogram model in equation (13) under the assumption of a number of targets per resolution cell ranging from 2 to 100. In all experiments the targets are uniformly deployed in a region from 0 m to 25 m, as indicated by the red rectangles. The height of ambiguity is fixed to 60 m in all experiments in the top row and 120 m in all experiments in the bottom row. Each histogram is obtained from 10^5 independent realizations. For sake of completeness, phase histograms were implemented in two ways: blue curves were obtained by accumulating unitary values, that is by letting $f_m = 1$ in equation (9); black curves were obtained by accumulating the interferogram amplitudes $|X|$, consistently with the methodology assumed in the analysis of experimental data.

It is readily observed that in all cases the phase histograms fail in reconstructing the simulated uniform distribution. In the case of 2 targets (left-hand panels) two peaks arise. The bimodal distribution arises from the actual value of the phase difference between the two targets $\psi_2 - \psi_1$ in each realization, determining the peak to show at $\frac{z_{max}}{2}$ or at $\frac{z_{max} - z_{amb}}{2}$.

When 3 or more targets are present the interferometric phase assumes a random behavior, and the resulting heights tend to distribute over the interval $\left(-\frac{z_{amb}}{2}, \frac{z_{amb}}{2}\right)$. Here, we observe that dispersion is minimized by forming phase histograms by accumulating the interferogram amplitudes, due to the fact that larger amplitudes are achieved by constructive interference when the random and deterministic terms in equation (13) are in phase. Still, we remark that in no case the shape of the phase histograms approaches the simulated uniform distribution. An interesting trait is that the observed height dispersion does not change dramatically with the number of simulated targets, nor by changing the height of the ambiguity. This observation suggests the possibility for an approximate determination of height dispersion in phase histograms depending on forest height solely. This topic is quantitatively considered in the following section.

A. Height dispersion in phase histograms

In this section we derive quantitative, yet reasonably simple, expressions to relate height dispersion in phase histograms to forest structure, aiming at providing results of practical use. To do that, we recall a well-known method from communication theory, consisting in evaluating the dispersion of the phase of a random complex number with real-valued expected value as the ratio of the dispersion of the imaginary part to the magnitude of the expected (see the Appendix). Please note that we neglect SAR signal extinction in the real illuminated scenario for sake of simplicity.

This result is translated to the case of a SAR interferogram as:

$$\sigma_\varphi = \frac{\sigma_{\Im\{X_c\}}}{|E[X]|} \tag{16}$$

where $X_c = X \cdot exp\left(-jk_z z_{pc}\right)$ is the counter-rotated interferogram, such that the phase of its expected value is 0 by construction. To compute the dispersion of the imaginary part we write X_c as:

$$X_c = \sum_{n=1}^{N_s} exp\left(jk_z\left(z_n - z_{pc}\right)\right) \cdot o_n \tag{17}$$

where N_s is the total number of scatterers per resolution cell, and o_n is defined as:

$$o_n = p_n + jq_n = exp\left(j\psi_n\right) \sum_{m=1}^{N_s} exp\left(-j\psi_m\right) \tag{18}$$

with p_n, q_n two random real-valued numbers. As per the last section, the target phases ψ_n are characterized as indepedent and identically distributed uniform variables in the interval $(-\pi, \pi)$.

It is immediate to show that $E[o_n] = 1$, after which one gets that $E[p_n] = 1$ and $E[q_n] = 0$. To calculate the second order moments of p_n, q_n we first calculate the expected values of the products $o_n o_m^*$ and $o_n o_m$:

$$E[o_n o_m^*] = \sum_{a=1}^{N_s} \sum_{b=1}^{N_s} E\left[exp\left(j\left(\psi_n - \psi_a - \psi_m + \psi_b\right)\right)\right] \tag{19}$$

As the phases ψ_n are assumed to be indepedent and identically distributed uniform variables in the interval $(-\pi, \pi)$, the expected value inside the sum can only be non-null when the four phases $\psi_n - \psi_a - \psi_m + \psi_b$ cancel out one another. If $n = m$, this requires that $a = b$, which happens N_s times. If $n \neq m$, it is required that $a = n$ and $b = m$, which can only happen one time. Accordingly, we get that:

$$E[o_n o_m^*] = (N_s - 1)\delta_{n-m} + 1 \tag{20}$$

where δ_{n-m} is the Kronecker delta. The expected value of $o_n o_m$ is:

$$E[o_n o_m] = \sum_{a=1}^{N_s} \sum_{b=1}^{N_s} E\left[exp\left(j\left(\psi_n - \psi_a + \psi_m - \psi_b\right)\right)\right] \tag{21}$$

If $n = m$, the condition for the four phases to cancel out is that $a = b = n$, which only happens once. If $n \neq m$, it is required that either $a = n$ and $b = m$ or that $a = m$ and $b = n$ which happens twice. Accordingly:

$$E[o_n o_m] = 2 - \delta_{n-m} \tag{22}$$

Noticing that:

$$E[o_n o_m^*] = E[p_n p_m] + E[q_n q_m] + jE[q_n p_m] - jE[p_n q_m] \tag{23}$$

$$E[o_n o_m] = E[p_n p_m] - E[q_n q_m] + jE[q_n p_m] + jE[p_n q_m] \tag{24}$$

it is immediate to see that $E[p_n q_m] = 0 \; \forall n, m$, as this is the one condition that makes both $E[o_n o_m^*]$ and $E[o_n o_m]$ real-valued, consistently with equation (20) and (22). At this point, the expected values of $p_n p_m$ and $q_n q_m$ are immediately obtained by taking the sum and the difference of equation (23) and (24):

$$E[p_n p_m] = \frac{E[o_n o_m^*] + E[q_n q_m]}{2} = \left(\frac{N_s}{2} - 1\right)\delta_{n-m} + \frac{3}{2} \tag{25}$$

$$E[q_n q_m] = \frac{E[o_n o_m^*] - E[q_n q_m]}{2} = \frac{N_s}{2}\delta_{n-m} - \frac{1}{2} \tag{26}$$

Finally, the covariances are obtained as: $Cov(p_n, p_m) = E[p_n p_m] - E[p_n]E[p_m]$, $Cov(q_n, q_m) = E[q_n q_m] - E[q_n]E[q_m]$. Since $E[p_n] = 1$ and $E[q_n] = 0$, we get that:

$$Cov(p_n, p_m) = \left(\frac{N_s}{2} - 1\right)\delta_{n-m} + \frac{1}{2}$$
$$Cov(q_n, q_m) = \frac{N_s}{2}\delta_{n-m} - \frac{1}{2} \tag{27}$$
$$Cov(p_n, q_m) = 0$$

for any n, m. After (17), the imaginary part of X_c is expressed as:

$$\Im(X_c) = \sum_{n=1}^{N_s} cos\left(k_z\left(z_n - z_{pc}\right)\right) \cdot q_n + sin\left(k_z\left(z_n - z_{pc}\right)\right) \cdot p_n \tag{28}$$

, and the variance of $\Im(X_c)$ is thus derived from (27) and (28) as:

$$\sigma^2_{\Im(X_c)} = \frac{N_s}{2}(N_s - 1) - \frac{1}{2}\left|\sum_{n=1}^{N_s} c_n\right|^2 + \frac{1}{2}\sum_{n=1}^{N_s} d_n \qquad (29)$$

where we put $c_n = cos(k_z(z_n - z_{pc}))$ and $d_n = cos(2k_z(z_n - z_{pc}))$ to simplify the notation. The phase variance is easily derived by noting that $E[X_C] = \sum_{n=1}^{N_s} c_n$, hence:

$$\sigma^2_\varphi = \frac{1}{2}\left[\frac{N_s(N_s - 1)}{\left|\sum_{n=1}^{N_s} c_n\right|^2} + \frac{\sum_{n=1}^{N_s} d_n}{\left|\sum_{n=1}^{N_s} c_n\right|^2} - 1\right] \qquad (30)$$

and height dispersion is finally obtained as:

$$\sigma_z = \frac{\sigma_\varphi}{k_z} \qquad (31)$$

The expressions above can be considerably simplified under the assumption of a large number of scatterers uniformly distributed over a total height z_{max}. In this case the following approximations hold:

$$\sum_{n=1}^{N_s} c_n \simeq N_s \cdot sinc\left(\frac{z_{max}}{z_{amb}}\right) \qquad (32)$$

$$\sum_{n=1}^{N_s} d_n \simeq N_s \cdot sinc\left(2\frac{z_{max}}{z_{amb}}\right)$$

Plugging (32) into (30) and neglecting terms that vanish for large N_s, one gets finally:

$$\sigma^2_\varphi \simeq \frac{1}{2}\left(sinc^{-2}\left(\frac{z_{max}}{z_{amb}}\right) - 1\right) \qquad (33)$$

after which height dispersion is approximated as:

$$\sigma_z \simeq \frac{1}{2\sqrt{2\pi}}\sqrt{z^2_{amb}\cdot\left(sinc^{-2}\left(\frac{z_{max}}{z_{amb}}\right) - 1\right)} \qquad (34)$$

Most interestingly, it is possible to show that σ_z converges to a non-null value as z_{amb} increases[2], leading to further approximating height dispersion as:

$$\sigma_z \simeq 0.2041 \cdot z_{max} \qquad (35)$$

which confirms the observation in the last section that height dispersion is mostly related to forest height[3].

The extent to within which the approximations in equations (34) and (35) are valid is investigated in Fig. 12, which reports height dispersion as a function of the number of targets per resolution cell for a uniform distribution of targets with $z_{max} = 25$ m. Three values of ambiguity are tested: 60 m, 80 m, and 150 m. Black curves result from Monte Carlo experiments simulating 10^5 realizations. Blue curves are drawn according to equation (31). Red circles are obtained from the approximation in equation (34). The limit predicted

---

[2]One can derive (35) by noting that $\lim\limits_{x\to 0}\left\{\frac{1}{2x^2}\left(sinc^{-2}(x) - 1\right)\right\} = \frac{\pi^2}{6}$.

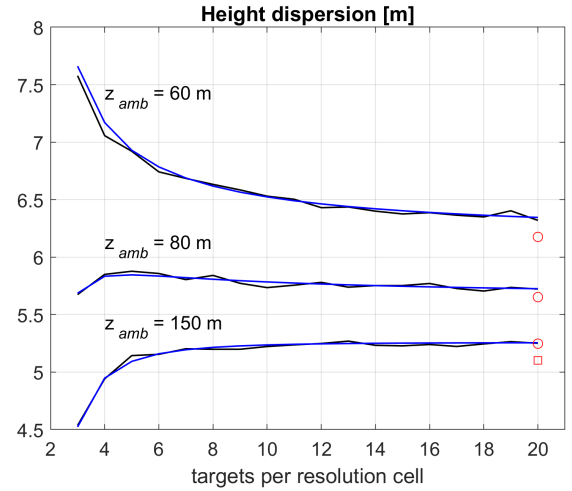[3]Neglecting noise or other decorrelation factors.

Fig. 12. Height dispersion in phase histograms as a function of the number of targets per resolution cell for a uniform distribution with $z_{max} = 25$ m. Black curves result from Monte Carlo experiments simulating 10^5 realizations. Blue curves are drawn according to equation (31). Red circles are obtained from the approximation in equation (34). The limit predicted by the approximation in equation (35) is $\sigma_z \simeq 5.1$ m and is indicated by the red square.

by the approximation in equation (35) is $\sigma_z \simeq 5.1$ m, as represented by the red square.

The approximation in equation (34) is observed to predict dispersion to within one meter or less whenever 4 or more targets are found within the resolution cell. The assessment in (35) is indeed not as accurate, especially for low values of the height of ambiguity. Yet, it succeeds in providing a first indication about height dispersion in phase histograms on the sole basis of forest height.

VI. DISCUSSION AND CONCLUSIONS

This paper has presented an evaluation using theoretical model and experimental results between SAR Tomography and the Phase Histogram technique in the context of remote sensing of forested areas. The analysis was initially carried out by applying both techniques to the analysis of L-Band tomographic data from the TomoSense campaign, flown in 2020 at the Eifel Park, North-West Germany. The observed results were then interpreted on the basis of a simple physical model to characterize phase histograms as a function of the number of scatterers per resolution cell, which led to an analytical assessment of the the expected outcome in terms of peak position and height dispersion.

Experimental results showed that phase histograms do provide some indication about forest structure, but are far from the accurate representation produced by SAR tomography. In particular: i) the ground signal could not be detected in phase histograms, whereas it was clearly visible in the tomograms with all polarizations; ii) the peak of the phase histogram along the vertical direction was generally observed to be at a lower location than the upper peak in the tomogram (hence below canopy height); iii) both single-look

and few-look phase histograms appear to be dispersed along the height direction; iv) no dramatic change was observed in the phase histogram by degrading spatial resolution from 6×1 m to 12×12 m (ground range×azimuth). According to the developed theory, the results are perfectly consistent with the presence of a distribution of elementary scatterers within each SAR resolution cell, in which conditions phase histograms cannot correctly reproduce forest vertical structure. From a physical point of view, we ascribe the observed behavior to a combination of L-Band penetration capabilities with the features of the TomoSense dataset, i.e.: medium spatial resolution (6 m in ground range) and hilly topography. Accordingly, one general conclusion from this work is that phase histograms cannot correctly reproduce forest vertical structure, *unless* Radar returns in each SAR pixel are actually determined by a dominant scatterer *and* the variation of the position of dominant scatterers in neighboring SAR pixels is large enough to probe the whole vertical structure. This can be in principle the case of very high-resolution data, preferably in the case where scattering from the terrain level is enhanced by a flat topography.

On the other hand, results relative to forest height retrieval show that tracking the upper envelope in phase histograms achieved an RMS error of 4.45 m and 5.46 m in NW and SW data, respectively. Whereas not as accurate as the results from tomography (2.8 m and 1.84 m in NW and SE data), those results advocate for the actual presence of strong, although not fully dominant, scatterers within each SAR pixel. Indeed, theoretical analysis showed that for a uniform distribution the main peak is expected to occur at half the forest height, with a dispersion slightly exceeding 20% of forest height. Were this the case for TomoSense, height retrieval from phase histograms would have shown significantly larger RMS errors (e.g.: for a 30 m uniformly distributed forest we would expect the peak to arise at 15 m, with a dispersion only slightly larger than 6 m). We remark that the observed accuracy is intended as a lower bound concerning phase histograms, since terrain topography was derived by tomography. Yet, these results confirm that the PH technique is a powerful method to retrieve forest height, especially considering that it can be implemented using just *two* acquisitions. In this sense, we reiterate our recommendation that the PH technique should be applied to high-resolution data, preferably paired with fully polarimetric acquisitions to help the detection of scattering from the terrain level using well-known PolInSAR methods.

APPENDIX A

The goal of this appendix is to describe how to evaluate the dispersion of the phase of a random complex number with real-valued expected value as the ratio of the dispersion of the imaginary part to the magnitude of the expected. The method is immediately understood by considering the problem of estimating the phase of a complex number in the presence of additive circle normal noise:

$$z = \rho e^{j\varphi} + w$$

We write z as $z = \hat{\rho} e^{j\hat{\varphi}}$, with $\hat{\rho}$ and $\hat{\varphi}$ the resulting magnitude and phase in the presence of noise. The phase estimation error due the presence of the additive noise is therefore $d\varphi = \hat{\varphi} - \varphi$. To relate the dispersion of $d\varphi$ to the the noise variance, we counter rotate z by the true phase φ:

$$z_C = z e^{-j\varphi} = \hat{\rho} e^{jd\varphi} = \rho + w_C \tag{36}$$

with $w_C = w e^{-j\varphi}$ the phase rotated noise. Assuming that the phase error is small, z_C can be linearized as:

$$z_C \simeq \rho + d\rho + j\rho d\varphi = \rho + \Re(w_C) + j\Im(w_C) \tag{37}$$

After which we have that

$$d\varphi = \frac{\Im(w_C)}{\rho} \tag{38}$$

APPENDIX B

The goal of this appendix is to describe more details of derivation from equation (27) to equation (29). we repeated the equation (28) of imagery part of the X_c.

$$\Im(X_c) = \sum_{n=1}^{N_s} cos\left(k_z\left(z_n - z_{pc}\right)\right)\cdot q_n + sin\left(k_z\left(z_n - z_{pc}\right)\right)\cdot p_n \tag{39}$$

For simplicity, we calculate the left and right parts of the equation (28) separately since they are unrelated:

$$A = \sum_{n=1}^{N_s} cos\left(k_z\left(z_n - z_{pc}\right)\right)\cdot q_n \tag{40}$$

$$B = \sum_{n=1}^{N_s} sin\left(k_z\left(z_n - z_{pc}\right)\right)\cdot p_n \tag{41}$$

Then, we can get the variances both two parts:

$$\begin{aligned}
\sigma_A^2 &= \sum_{n,m}^{N_s} c_n c_m \cdot \left(\frac{N_s}{2}\delta_{n-m} - \frac{1}{2}\right) \\
&= \sum_{n=m}^{N_s} c_n^2 \frac{N_s}{2} - \frac{1}{2}\sum_{n,m}^{N_s} c_n c_m \\
&= \sum_{n=m}^{N_s} c_n^2 \frac{N_s}{2} - \frac{1}{2}\left|\sum_{n}^{N_s} c_n\right|^2
\end{aligned} \tag{42}$$

$$\begin{aligned}
\sigma_B^2 &= \sum_{n,m}^{N_s} s_n s_m \cdot \left(\left(\frac{N_s}{2} - 1\right)\delta_{n-m} + \frac{1}{2}\right) \\
&= \sum_{n=m}^{N_s} s_n^2 \left(\frac{N_s}{2} - 1\right) + \frac{1}{2}\sum_{n,m}^{N_s} s_n s_m \\
&= \sum_{n=m}^{N_s} s_n^2 \frac{N_s}{2} - \sum_{n=m}^{N_s} s_n^2 + \frac{1}{2}\sum_{n,m}^{N_s} s_n s_m
\end{aligned} \tag{43}$$

where we put $c_n = cos\left(k_z\left(z_n - z_{pc}\right)\right)$, $s_n = sin\left(k_z\left(z_n - z_{pc}\right)\right)$ and $d_n = cos\left(2k_z\left(z_n - z_{pc}\right)\right)$ to simplify the notation. For any n, m, the counter-rotation makes the expected value of interferogram a real number, resulting in $\sum_{n,m}^{N_s} s_n s_m = 0$. Then the variance of $\Im(X_c)$ is thus derived from equation (42) and (43),

$$\sigma^2_{\Im(X_c)} = \sigma^2_A + \sigma^2_B$$

$$= \sum_{n=m}^{N_s} c_n^2 \frac{N_s}{2} - \frac{1}{2}\left|\sum_{n}^{N_s} c_n\right|^2 + \sum_{n=m}^{N_s} s_n^2 \frac{N_s}{2} - \sum_{n=m}^{N_s} s_n^2$$

$$= \sum_{n=m}^{N_s} \left(c_n^2 + s_n^2\right)\frac{N_s}{2} - \frac{1}{2}\left|\sum_{n}^{N_s} c_n\right|^2 - \frac{1}{2}\sum_{n}^{N_s}\left(1 - d_n\right)$$

$$= \frac{N_s}{2}\left(N_s - 1\right) - \frac{1}{2}\left|\sum_{n=1}^{N_s} c_n\right|^2 + \frac{1}{2}\sum_{n=1}^{N_s} d_n \tag{44}$$

ACKNOWLEDGMENT

REFERENCES

[1] S. World Meteorological Organization (WMO); United Nations Environment Programme (UNEP) ; International Council of Scientific Unions (ICSU) ; Intergovernmental Oceanographic Commission of the United Nations Educational and C. O. (IOC-UNESCO), "The global observing system for climate: Implementation needs," 04 2016.

[2] J. M. Bruening, R. Fischer, F. J. Bohn, J. Armston, A. H. Armstrong, N. Knapp, H. Tang, A. Huth, and R. Dubayah, "Challenges to aboveground biomass prediction from waveform lidar," *Environ. Res. Lett.*, vol. 16, no. 12, p. 125013, dec 2021. [Online]. Available: https://dx.doi.org/10.1088/1748-9326/ac3cec

[3] A. Baccini, S. J. Goetz, W. S. Walker, N. T. Laporte, M. Sun, D. Sulla-Menashe, J. Hackler, P. S. Beck, R. Dubayah, M. A. Friedl, S. Samanta, and R. A. Houghton, "Estimated carbon dioxide emissions from tropical deforestation improved by carbon-density maps," *Nat. Clim. Chang.*, vol. 2, no. 3, pp. 182–185, mar 2012.

[4] S. Quegan, T. Le Toan, J. Chave, J. Dall, J. F. Exbrayat, D. H. T. Minh, M. Lomas, M. M. D'Alessandro, P. Paillou, K. Papathanassiou, F. Rocca, S. Saatchi, K. Scipal, H. Shugart, T. L. Smallman, M. J. Soja, S. Tebaldini, L. Ulander, L. Villard, and M. Williams, "The European Space Agency BIOMASS mission: Measuring forest aboveground biomass from space," *Remote Sens. Environ.*, vol. 227, pp. 44–60, jun 2019.

[5] R. N. Treuhaft and P. R. Siqueira, "Vertical structure of vegetated land surfaces from interferometric and polarimetric radar," *Radio Sci.*, vol. 35, no. 1, pp. 141–177, jan 2000.

[6] K. P. Papathanassiou and S. R. Cloude, "Single-baseline polarimetric SAR interferometry," *IEEE Trans. Geosci. Remote Sens.*, vol. 39, no. 11, pp. 2352–2363, nov 2001.

[7] S. Tebaldini, "Algebraic synthesis of forest scenarios from multibaseline PolInSAR data," *IEEE Trans. Geosci. Remote Sens.*, vol. 47, no. 12, pp. 4132–4142, dec 2009.

[8] C. Wu, C. Wang, P. Shen, J. Zhu, H. Fu, and H. Gao, "Forest Height Estimation Using PolInSAR Optimal Normal Matrix Constraint and Cross-Iteration Method," *IEEE Geosci. Remote Sens. Lett*, vol. 16, no. 8, pp. 1245–1249, 2019.

[9] M. D. Mariotti Dalessandro, S. Tebaldini, S. Quegan, M. J. Soja, L. M. Ulander, and K. Scipal, "Interferometric Ground Cancellation for above Ground Biomass Estimation," *IEEE Trans. Geosci. Remote Sens.*, vol. 58, no. 9, pp. 6410–6419, sep 2020.

[10] M. J. Soja, S. Quegan, M. M. D'Alessandro, F. Banda, K. Scipal, S. Tebaldini, and L. M. Ulander, "Mapping above-ground biomass in tropical forests with ground-cancelled P-band SAR and limited reference data," *Remote Sens. Environ.*, vol. 253, 2020.

[11] A. Reigber and A. Moreira, "First demonstration of airborne SAR tomography using multibaseline L-band data," *IEEE Trans. Geosci. Remote Sens.*, vol. 38, no. 5 I, pp. 2142–2152, sep 2000.

[12] S. Tebaldini, D. Ho Tong Minh, M. Mariotti d'Alessandro, L. Villard, T. Le Toan, and J. Chave, "Evaluating p-band tomosar for biomass retrieval in boreal forest," *Surv Geophys*, vol. 40, no. 5, pp. 779–801, 2019.

[13] S. Tebaldini and F. Rocca, "Multibaseline polarimetric SAR tomography of a boreal forest at P- and L-Bands," *IEEE Trans. Geosci. Remote Sens.*, vol. 50, no. 1, pp. 232–246, jan 2012.

[14] G. Martín Del Campo, M. Nannini, and A. Reigber, "Towards Feature Enhanced SAR Tomography: A Maximum-Likelihood Inspired Approach," *IEEE Geosci. Remote Sens. Lett*, vol. 15, no. 11, pp. 1730–1734, nov 2018.

[15] V. Cazcarra-Bes, M. Pardini, M. Tello, and K. P. Papathanassiou, "Comparison of Tomographic SAR Reflectivity Reconstruction Algorithms for Forest Applications at L-band," *IEEE Trans. Geosci. Remote Sens.*, vol. 58, no. 1, pp. 147–164, jan 2020.

[16] Y. Yu, M. M. D'Alessandro, S. Tebaldini, and M. Liao, "Signal processing options for high resolution SAR tomography of natural scenarios," *Remote Sens.*, vol. 12, no. 10, may 2020.

[17] S. Tebaldini, M. M. d'Alessandro, L. M. Ulander, P. Bennet, A. Gustavsson, A. Coccia, K. Macedo, M. Disney, P. Wilkes, H.-J. Spors *et al.*, "Tomosense: A unique 3d dataset over temperate forest combining multi-frequency mono-and bi-static tomographic sar with terrestrial, uav and airborne lidar, and in-situ forest census," *Remote Sens. Environ.*, vol. 290, p. 113532, 2023.

[18] M. Mariotti d'Alessandro and S. Tebaldini, "Digital terrain model retrieval in tropical forests through p-band sar tomography," *IEEE Trans. Geosci. Remote Sens.*, vol. 57, no. 9, pp. 6774–6781, 2019.

[19] V. Wasik, P. C. Dubois-Fernandez, C. Taillandier, and S. S. Saatchi, "The afrisar campaign: Tomographic analysis with phase-screen correction for p-band acquisitions," *IEEE J. Sel. Topics Appl. Earth Observ. Remote Sens.*, vol. 11, no. 10, pp. 3492–3504, 2018.

[20] M. Pardini, M. Tello, V. Cazcarra-Bes, K. P. Papathanassiou, and I. Hajnsek, "L- A nd P-band 3-D SAR reflectivity profiles versus lidar waveforms: The AfriSAR case," *IEEE J. Sel. Topics Appl. Earth Observ. Remote Sens.*, vol. 11, no. 10, pp. 3386–3401, oct 2018.

[21] D. Ho Tong Minh, T. Le Toan, F. Rocca, S. Tebaldini, M. M. D'Alessandro, and L. Villard, "Relating P-band synthetic aperture radar tomography to tropical forest biomass," *IEEE Trans. Geosci. Remote Sens.*, vol. 52, no. 2, pp. 967–979, feb 2014.

[22] D. Ho Tong Minh, T. Le Toan, F. Rocca, S. Tebaldini, L. Villard, M. Réjou-Méchain, O. L. Phillips, T. R. Feldpausch, P. Dubois-Fernandez, K. Scipal, and J. Chave, "SAR tomography for the retrieval of forest biomass and height: Cross-validation at two tropical forest sites in French Guiana," *Remote Sens. Environ.*, vol. 175, pp. 138–147, mar 2016.

[23] E. Blomberg, L. Ferro-Famil, M. J. Soja, L. M. H. Ulander, and S. Tebaldini, "Forest biomass retrieval from l-band sar using tomographic ground backscatter removal," *IEEE Geosci. Remote Sens. Lett*, vol. 15, no. 7, pp. 1030–1034, 2018.

[24] E. Blomberg, L. M. H. Ulander, S. Tebaldini, and L. Ferro-Famil, "Evaluating p-band tomosar for biomass retrieval in boreal forest," *IEEE Trans. Geosci. Remote Sens.*, vol. 59, no. 5, pp. 3793–3804, 2021.

[25] C. Wu, X. Yang, Y. Yu, S. Tebaldini, L. Zhang, and M. Liao, "Assessment of underlying topography and forest height inversion based on TomoSAR methods," *Geo-Spat. Inf. Sci.*, vol. 0, no. 0, pp. 1–16, 2022. [Online]. Available: https://doi.org/10.1080/10095020.2022.2083985

[26] R. N. Treuhaft, B. D. Chapman, J. R. Dos Santos, F. G. Gonçalves, L. V. Dutra, P. M. Graça, and J. B. Drake, "Vegetation profiles in tropical forests from multibaseline interferometric synthetic aperture radar, field, and lidar measurements," *J. Geophys. Res. Atmos.*, vol. 114, no. 23, 2009.

[27] Y. Lei, R. Treuhaft, and F. Gonçalves, "Automated estimation of forest height and underlying topography over a Brazilian tropical forest with single-baseline single-polarization TanDEM-X SAR interferometry," *Remote Sens. Environ.*, vol. 252, jan 2021.

[28] G. H. Shiroma and M. Lavalle, "Digital Terrain, Surface, and Canopy Height Models from InSAR Backscatter-Height Histograms," *IEEE Trans. Geosci. Remote Sens.*, vol. 58, no. 6, pp. 3754–3777, jun 2020.

[29] S. Tebaldini, F. Rocca, M. Mariotti D'Alessandro, and L. Ferro-Famil, "Phase calibration of airborne tomographic SAR data via phase center double localization," *IEEE Trans. Geosci. Remote Sens.*, vol. 54, no. 3, pp. 1775–1792, mar 2016.

[30] M. Pardini, M. Tello, V. Cazcarra-Bes, K. P. Papathanassiou, and I. Hajnsek, "L- and p-band 3-d sar reflectivity profiles versus lidar waveforms: The afrisar case," *IEEE J. Sel. Topics Appl. Earth Observ. Remote Sens.*, vol. 11, no. 10, pp. 3386–3401, 2018.

[31] V. Wasik, P. C. Dubois-Fernandez, C. Taillandier, and S. S. Saatchi, "The afrisar campaign: Tomographic analysis with phase-screen correction for p-band acquisitions," *IEEE J. Sel. Topics Appl. Earth Observ. Remote Sens.*, vol. 11, no. 10, pp. 3492–3504, 2018.

[32] G. Fornaro, F. Serafino, and F. Soldovieri, "Three-dimensional focusing with multipass SAR data," *IEEE Trans. Geosci. Remote Sens.*, vol. 41, no. 3, pp. 507–517, March 2003.

[33] G. Fornaro, F. Lombardini, and F. Serafino, "Three-dimensional multi-pass SAR focusing: experiments with long-term spaceborne data," *IEEE Trans. Geosci. Remote Sens.*, vol. 43, no. 4, pp. 702–714, April 2005.

[34] H. Joerg, M. Pardini, I. Hajnsek, and K. P. Papathanassiou, "3-d scattering characterization of agricultural crops at c-band using sar tomography," *IEEE Trans. Geosci. Remote Sens.*, vol. 56, no. 7, pp. 3976–3989, 2018.

[35] Y. Huang, L. Ferro-Famil, and A. Reigber, "Under-foliage object imaging using sar tomography and polarimetric spectral estimators," *IEEE Trans. Geosci. Remote Sens.*, vol. 50, no. 6, pp. 2213–2225, June 2012.

[36] S. Tebaldini, T. Nagler, H. Rott, and A. Heilig, "Imaging the internal structure of an alpine glacier via l-band airborne sar tomography," *IEEE Trans. Geosci. Remote Sens.*, vol. 54, no. 12, pp. 7197–7209, Dec 2016.

[37] T. G. Yitayew, L. Ferro-Famil, T. Eltoft, and S. Tebaldini, "Tomographic imaging of fjord ice using a very high resolution ground-based sar system," *IEEE Trans. Geosci. Remote Sens.*, vol. 55, no. 2, pp. 698–714, 2017.

[38] B. Rekioua, M. Davy, L. Ferro-Famil, and S. Tebaldini, "Snowpack permittivity profile retrieval from tomographic sar data," *Comptes Rendus Physique*, vol. 18, no. 1, pp. 57–65, 2017, prizes of the French Academy of Sciences 2015 / Prix de l'Académie des sciences 2015. [Online]. Available: https://www.sciencedirect.com/science/article/pii/S1631070515002947

[39] H. Aghababaei, G. Ferraioli, L. Ferro-Famil, Y. Huang, M. Mariotti D'Alessandro, V. Pascazio, G. Schirinzi, and S. Tebaldini, "Forest SAR Tomography: Principles and Applications," *IEEE Geosci. Remote Sens Mag.*, vol. 8, no. 2, pp. 30–45, jun 2020.

[40] X. X. Zhu and R. Bamler, "Very high resolution spaceborne sar tomography in urban environment," *IEEE Trans. Geosci. Remote Sens.*, no. 99, pp. 1–13, 2010.

[41] F. Lombardini, "Differential tomography: a new framework for sar interferometry," *IEEE Trans. Geosci. Remote Sens.*, vol. 43, no. 1, pp. 37–44, Jan 2005.

[42] F. Gini, F. Lombardini, and M. Montanari, "Layover solution in multi-baseline SAR interferometry," *Aerospace and Electronic Systems, IEEE Transactions on*, vol. 38, no. 4, pp. 1344–1356, Oct 2002.

[43] S. Tebaldini and F. Rocca, "Multibaseline polarimetric sar tomography of a boreal forest at P- and L-bands," *IEEE Trans. Geosci. Remote Sens.*, vol. 50, no. 1, pp. 232 –246, jan. 2012.

[44] H. A. Zebker, J. Villasenor *et al.*, "Decorrelation in interferometric radar echoes," *IEEE Trans. Geosci. Remote Sens.*, vol. 30, no. 5, pp. 950–959, 1992.

[45] A. Monti-Guarnieri, M. Manzoni, D. Giudici, A. Recchia, and S. Tebaldini, "Vegetated target decorrelation in sar and interferometry: Models, simulation, and performance evaluation," *Remote Sens.*, vol. 12, no. 16, 2020. [Online]. Available: https://www.mdpi.com/2072-4292/12/16/2545

[46] Y. Bai, S. Tebaldini, D. H. T. Minh, and W. Yang, "An empirical study on the impact of changing weather conditions on repeat-pass sar tomography," *IEEE J. Sel. Topics Appl. Earth Observ. Remote Sens.*, vol. 11, no. 10, pp. 3505–3511, 2018.

[47] D. Ho Tong Minh, S. Tebaldini, F. Rocca, T. Le Toan, P. Borderies, T. Koleck, C. Albinet, A. Hamadi, and L. Villard, "Vertical structure of p-band temporal decorrelation at the paracou forest: Results from tropiscat," *IEEE Geosci. Remote Sens. Lett*, vol. 11, no. 8, pp. 1438–1442, 2014.

[48] D. Ho Tong Minh, S. Tebaldini, F. Rocca, and T. Le Toan, "The impact of temporal decorrelation on biomass tomography of tropical forests," *IEEE Geosci. Remote Sens. Lett*, vol. 12, no. 6, pp. 1297–1301, 2015.

[49] R. Treuhaft, F. Gonçalves, J. R. dos Santos, M. Keller, M. Palace, S. N. Madsen, F. Sullivan, and P. M. L. A. Graça, "Tropical-forest biomass estimation at x-band from the spaceborne tandem-x interferometer," *IEEE Geosci. Remote Sens. Lett*, vol. 12, no. 2, pp. 239–243, 2015.

[50] F. De Zan, G. Krieger, and P. Lopez-Dekker, "On some spectral properties of tandem-x interferograms over forested areas," *IEEE Geosci. Remote Sens. Lett.*, vol. PP, no. 99, pp. 1 –5, 2012.

[51] M. Mariotti d'Alessandro, S. Tebaldini, and F. Rocca, "Phenomenology of ground scattering in a tropical forest through polarimetric synthetic aperture radar tomography," *IEEE Trans. Geosci. Remote Sens.*, vol. 51, no. 8, pp. 4430–4437, 2013.